Supplementary Information

Gate Dielectric-Induced Lattice Strain and Band Gap Tuning in Van der Waals 2D Semiconducting Channel

Manpreet Kaur, Km Neeshu, Jyoti Saini, Tapaswini Dash, Akash Kumar Maharana, Kiran S. Hazra*

Institute of Nano Science and Technology, Sector-81, Knowledge City, SAS Nagar, Punjab 140306, India.

*Email: kiran@inst.ac.in

Section S1: Calculation gate electric field

The gate electric field is calculated using the following relation[1,2]: $E = -\frac{V}{d}\hat{n}$

where V corresponds to the applied gate voltage, which varies from -120 V to +120 V; and d is separation between the two ITO-coated PET electrodes through the gate dielectric medium. $\hat{n}$ is unit vector pointing from negative to positive. For the air gate dielectric, the separation between the electrodes is ~1 mm, resulting in a gate electric field ranging from 0 to 120 kV m^{-1}. For the hBN gate dielectric, with a separation of ~200 nm between the electrodes, the electric field varies from 0 to 600 MV m^{-1}.

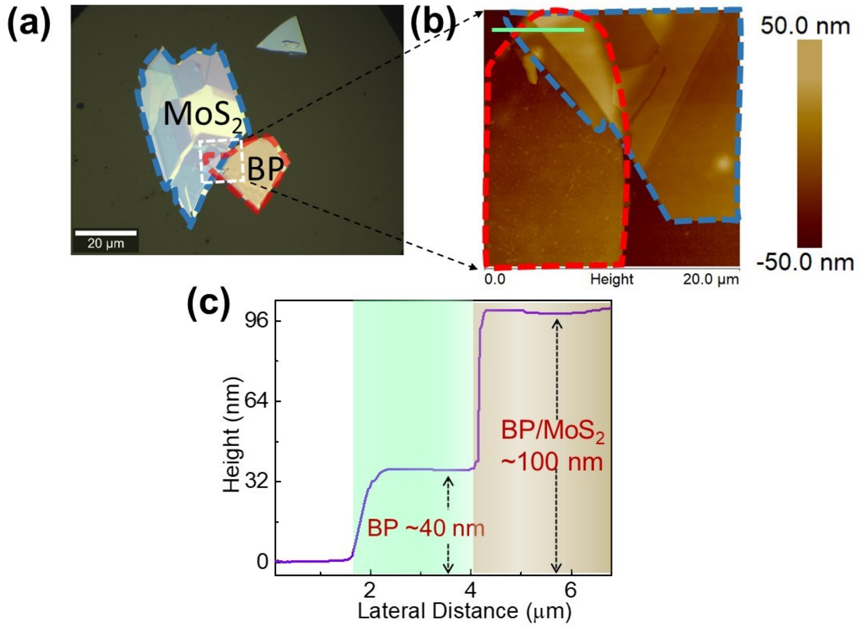

Figure S1: Thickness characterization of BP/MoS_2 heterostructure. (a) Optical micrograph of the BP/MoS_2 device. (b) Atomic force microscopy (AFM) image at the heterointerface (indicated by the white-marked region in the optical micrograph). (c) Height profile of the heterostructure measured along the green-marked region in the AFM image. The blue-marked region corresponds to the MoS_2 flake, while the red-marked region corresponds to the BP flake.

Section S2: Analysis of the height profile in van der Waals 2D semiconducting channel

As per the measurements shown in Figure S1 (Optical micrograph in Figure S1a and AFM image in Figure S1b), we have performed height profile analysis[3,4] for each layer in the heterostructure. Specifically, the MoS_2 layer exhibits a thickness of ~60 nm, while the BP layer is around ~40 nm thick. At the interface, the combined thickness of the BP/MoS_2 heterostructure is ~100 nm. Further, hBN/BP/MoS_2 heterostructure device is fabricated using dry transfer (Figure S2). Figure S2a shows an optical micrograph of the prepared heterostructure, while the atomic force microscopy (AFM) morphology image in Figure S2b indicates height~200 nm at the hetero-interface.

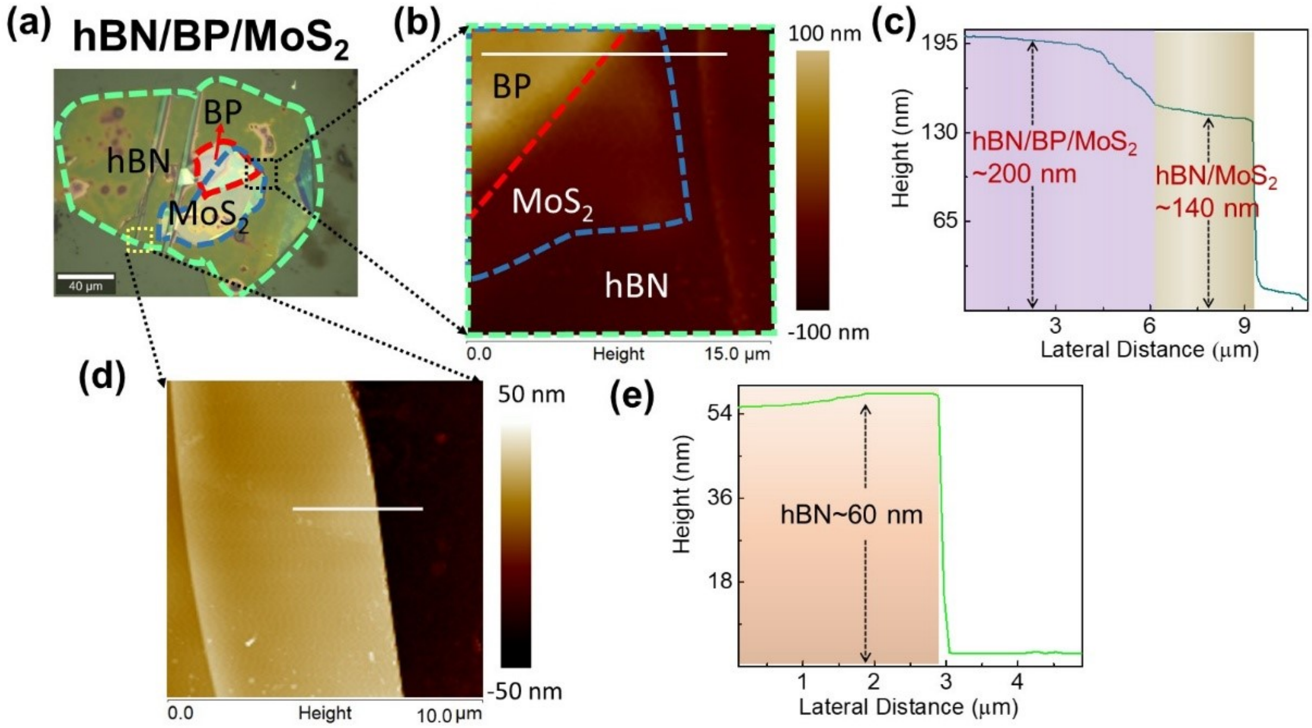

Figure S2: Thickness characterization of hBN/BP/MoS_2 heterostructure device. (a) Optical micrograph of the device. (b) Atomic force microscopy (AFM) image at the heterointerface (indicated by the blacked-marked region in the optical micrograph). (c) Height profile of the heterostructure measured along the white-marked region in the AFM image. The blue and green marked region corresponds to the MoS_2 and hBN flakes, while the red-marked region corresponds to the BP flake. (d) AFM image of hBN layer yellow-marked region in the optical micrograph). (e) Height profile of hBN flake the heterostructure along the white-marked region in the AFM image.

Section S3: Comparison of Raman spectra of BP, MoS_2, and BP/MoS_2 heterostructure devices

The Raman spectrum of MoS_2 (Figure S3), with peaks at 381.5 cm^{-1} and 408.9 cm^{-1}, representing the E_{2g}^1 (in-plane optical vibration of molybdenum and sulfur atoms) and A_{1g} (out-of-plane optical vibration of sulfur atoms) active vibrational modes. The frequency difference between these two characteristic modes of MoS_2 is ~27.4 cm^{-1}, indicating a multilayer nature. In which peaks at 362.4 cm^{-1}, 437.8 cm^{-1}, and 465 cm^{-1} correspond to the A_g^1 (out-of-plane), B_{2g} (in-plane vibration along the zigzag direction), and A_g^2 (in-plane vibration along the armchair direction) vibrational modes of BP, respectively. The Raman spectrum at the interface of the BP/MoS2 heterostructure channel combines the active modes of both MoS_2 and BP layers, which confirms the formation of the heterostructure.

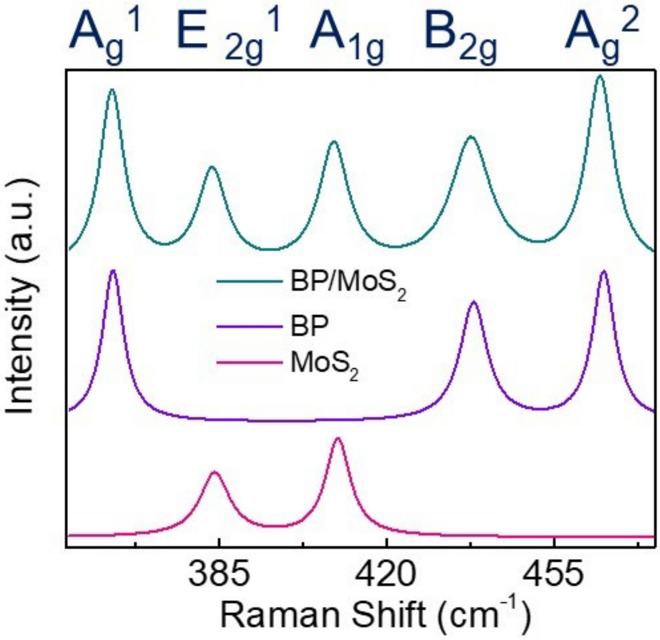

Figure S3: Raman spectra of BP, MoS_2, and BP/MoS_2 heterostructure devices

Section S4: Normalization of the vibrational modes of 2D semiconductor devices with different gate dielectric under varying gate voltages

The normalization allows for a clearer comparison of the vibrational modes under varying gate voltages, which is crucial for interpreting the effects of positive and negative gate voltages on the phonon modes of the material. The effect of positive and negative gate voltages varies with the orientation of a pristine material exhibiting symmetry. This is particularly relevant in materials where the electronic and phononic properties are sensitive to external perturbations, such as electric fields. When a gate voltage is applied, it alters the electronic environment, that can lead to asymmetrical shifts in phonon modes. This phenomenon is particularly relevant in materials such as black phosphorus MoS_2 and other 2D materials, where the vibrational modes exhibit distinct characteristics based on the applied electric field.[5]

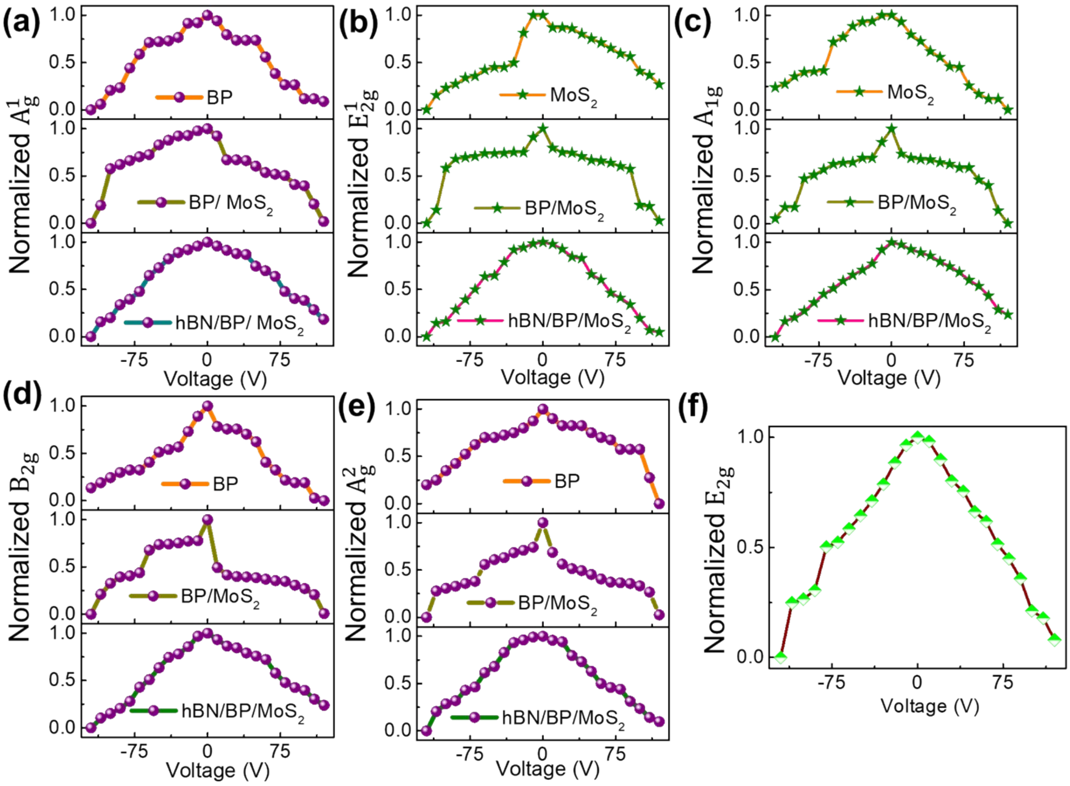

Figure S4. Variation of Normalised Raman shift for the vibrational modes: (a) $A^1{}_g$ (b) $E_{2g}{}^1$ (c) A_{1g} (d) B_{2g} (e) $A^2{}_g$ and (f) E_{2g} of BP, MoS_2, BP/MoS_2, and hBN/BP/MoS_2 devices as a function of applied gate voltage through dielectric around the junction.

The asymmetry observed in the vibrational modes, suggests that the material's response to electric fields is not uniform, which can be attributed to factors such as stacking order, charge trapping, and local strain.[6] For instance, the coupling of phonons to charge carriers can lead to shifts in the phonon frequencies, which may be observed as asymmetric peaks in Raman spectra.[7] In our study, we observed that the out-of-plane vibrational modes exhibited asymmetry, alongside some asymmetry in the B_{2g} modes. This observation aligns with findings in the literature where similar asymmetries have been attributed to the influence of defects and local strain on phonon behavior.[8] The presence of defects can localize phonon modes, leading to shifts in their frequencies and broadening of the Raman peaks, which is consistent with the behavior we observed in our experiments.[9] Moreover, the asymmetry in the phonon modes can be quantitatively analyzed through the Fano resonance effect, which is known to occur in systems with strong electron-phonon coupling.[10] This phenomenon can provide a deeper understanding of the interactions between the phonons and the electronic states, particularly in the context of layered materials where interlayer interactions play a significant role.[11,12] Also, the electron-phonon interactions in van der Waals heterostructures are highly sensitive to the material's symmetry and stacking order.[13] Chen et al.[14] demonstrate that materials with orthorhombic lattice structures, such as black phosphorus and SnSe, exhibit anisotropic optical and electronic properties that differ from those of transition metal dichalcogenides (TMDs). This anisotropy can lead to distinct shifts in Raman modes when subjected to positive and negative gate voltages, revealing the intricate relationship between electronic states and vibrational modes.

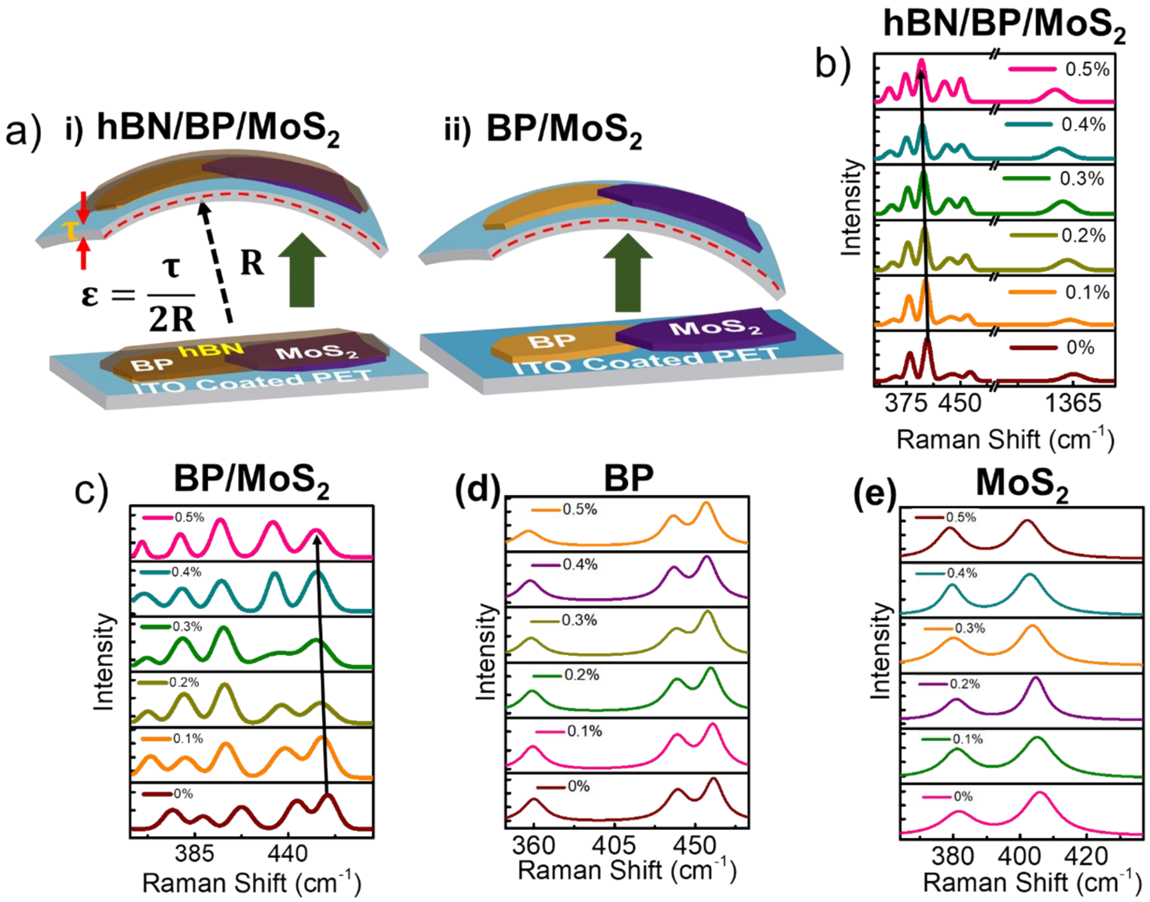

Figure S5: Characteristic phonon vibrational modes of van der waal 2D materials such as hBN/BP/MoS$_2$ heterostructure, BP/MoS$_2$ heterostructure, MoS$_2$, BP under uniaxial strain. (a) A schematic of our bending system used to uniaxial strain the devices and measure the vibrational phonon modes. Evolution of the Raman spectra of (b) hBN/BP/MoS$_2$

heterostructure, (c) BP/MoS_2 heterostructure, (d) MoS_2, (e) BP under uniaxial strain from 0% to 0.5%.

Section S5: How to calculate the perturbation under the applied voltage?

We explored how the Raman spectra of van der Waals 2D materials, like hBN/BP/MoS_2 and BP/MoS_2 heterostructures, MoS_2, and BP, evolve under uniaxial strain, as shown in Figure S5. To do this, we transferred these materials onto a flexible ITO/PET substrate. This setup allowed us to observe the effects of uniaxial strain-induced interlayer interactions, which can influence the vibrations of phonon modes in heterostructures. The uniaxial strain applied was calculated using $\varepsilon = \tau/R$, where 2τ represents the thickness of the PET substrate (100 µm), and R is the radius of curvature, as depicted in Figure S5a. The experimental setup employed for applying uniaxial strain and acquiring Raman spectra is schematically illustrated in Figure S5a. The evolution of characteristic phonon vibrational modes under increasing strain (0%–0.5%) is presented in Figures S5b–e for hBN/BP/MoS_2, BP/MoS_2, BP, and MoS_2, respectively. In Figure S5b, we present the uniaxial strain dependence of the Raman spectra obtained from the devices transferred onto the PET substrate under uniaxial strain. We observed shifts in the vibration modes of all devices under uniaxial strain, as shown in Figure S6.

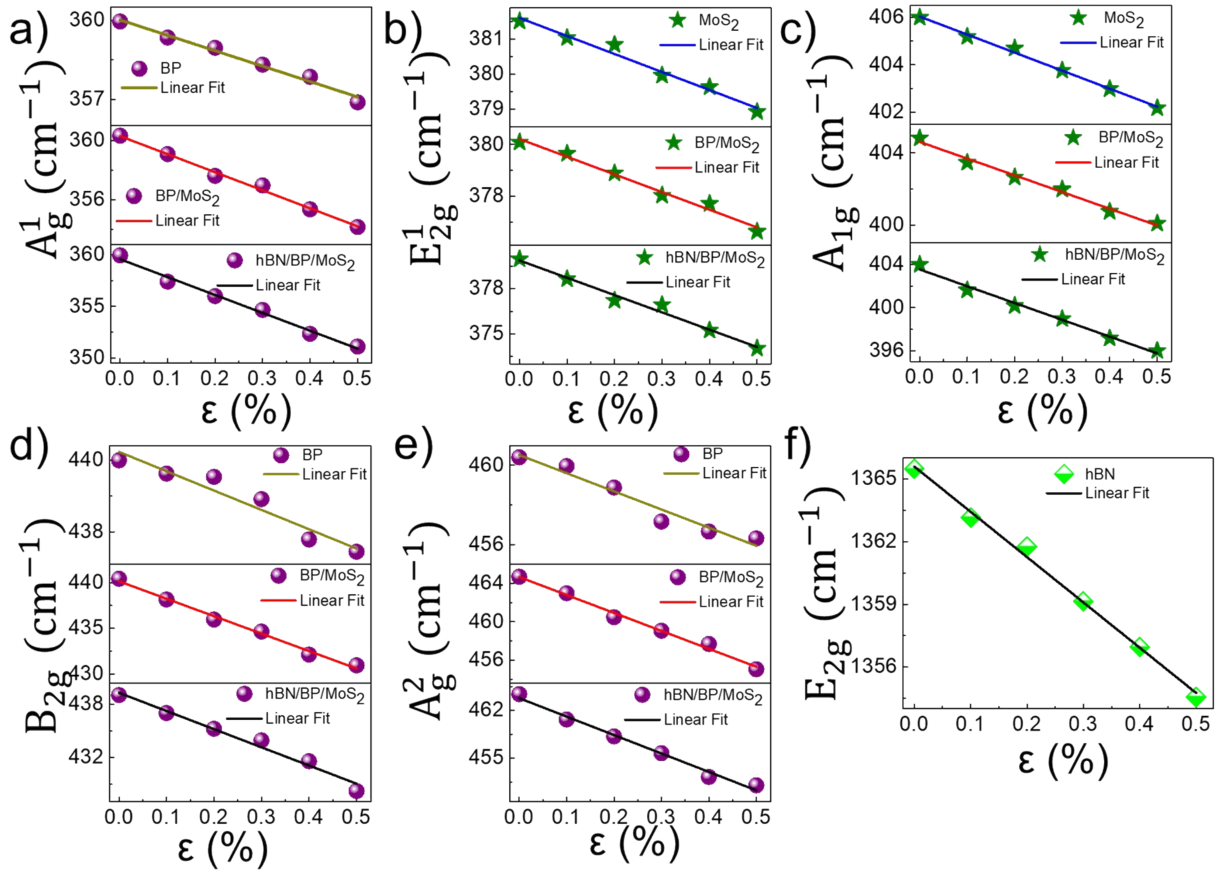

Figure S6. The change in the vibrational modes: (a) A^1_g (b) $E_{2g}{}^1$ (c) A_{1g} (d) B_{2g} (e) A^2_g and (f) E_{2g} of BP, MoS2, BP/MoS_2, and hBN/BP/MoS_2 devices under uniaxial strain.

The Raman shift of vibrational modes is influenced by both strain and temperature, which must be considered for an accurate estimation of the strain-induced frequency shift. The temperature and strain dependence of the phonon modes is expressed as:

$$\omega_{E_{2g}^1} = 2 * \gamma_{E_{2g}^1} * \varepsilon + c_{0_{E_{2g}^1}} + c_{1_{E_{2g}^1}} * T \tag{1}$$

$$\omega_{A_{1g}} = 2 * \gamma_{A_{1g}} * \varepsilon + c_{0A_{1g}} + c_{1A_{1g}} * T \tag{2}$$

Where γ is Grüneisen parameter for vibrational modes, c_0 and c_1 are constant and T is temperature during the measurement.

For our experiments, the measurements were performed at room temperature, T = 25°C = 298 K, Therefore, Equation (1) becomes:

$$\omega_{E_{2g}^1} = 2 * \gamma_{E_{2g}^1} * \varepsilon + c_{0_{E_{2g}^1}} + c_{1_{E_{2g}^1}} * 298$$

$$\omega_{E_{2g}^1} = 2 * \gamma_{E_{2g}^1} * \varepsilon + C' \tag{3}$$

To extract the Grüneisen parameter, we perform a series of Raman measurements at different strain levels (while maintaining a constant temperature) and then employ a linear fit to determine the slope $\frac{\partial \omega}{\partial \varepsilon}$ (as shown in **Figure S6**). The Grüneisen parameter is then calculated using the relation:[15,16]

$$\gamma = -\frac{1}{\omega_0}\frac{\partial \omega}{\partial \varepsilon} \tag{4}$$

where ω_0-initial frequency of vibrational mode without uniaxial strain and ω-frequency at different uniaxial strain. The calculated values of γ for different phonon modes across the four vdW devices are summarized in Table S1. We observed a higher Grüneisen parameter for the van der Waals hBN/BP/MoS_2 heterostructure compared to other van der Waals devices (BP/MoS_2 heterostructure, MoS_2, BP), indicating that the dielectric hBN induces lattice perturbations in the 2D crystal structure.

Table S1: Comparison of γ-Grüneisen parameter for vibrational modes in the four devices

Peaks	A_g^1	E_{2g}^1	A_{1g}	B_{2g}	A_g^2	$\mathbf{E_{2g}}$
$\gamma_{\mathrm{hBN/BP/MoS2}}$	**4.8**	**3.04**	**3.8**	**4.7**	**5.8**	**1.59**

$\gamma_{BP/MoS2}$	**3.4**	**1.8**	**2.3**	**4.34**	**4.03**	**-**
γ_{BP}	**1.6**	**-**	**-**	**1.22**	**1.99**	**-**
γ_{MoS2}	**-**	**1.4**	**1.9**	**-**	**-**	**-**

Section S6: Induced strain on the channel, mediated by the gate dielectric and its electric field

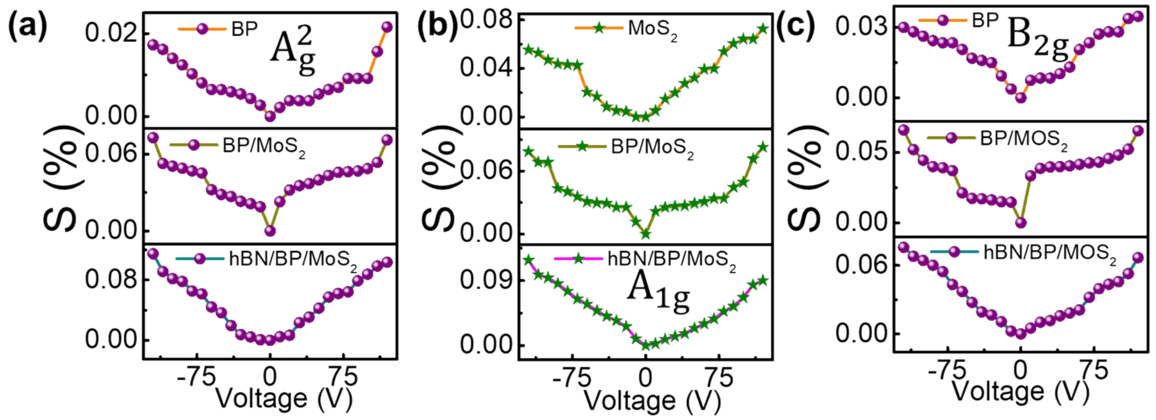

Figure S7. Evaluation of induced strain (S) for the vibrational modes: (a) A^2_g (b) A_{1g} and (c) B_{2g} of BP, MoS_2, BP/MoS_2, and hBN/BP/MoS_2 devices under applied gate voltage at the junction.

References

1. G. W. Parker, *Am. J. Phys.*, 2002, 70, 502–507.
2. V. A. Tishchenko, V. I. Tokatly and V. I. Lukyanov, *Meas. Technol.*, 2012, 55, 459–462.
3. G. Lee, et al., *ACS Appl. Mater. Interfaces*, 2018, 10, 10347–10352.
4. Y. Deng, et al., *ACS Nano*, 2014, 8, 8292–8299.
5. N. Mao, J. Wu, B. Han, J. Lin, L. Tong and J. Zhang, *Small*, 2016, 12, 2627–2633.
6. M. Chen, Y. Wang, C. Huang, W. Wang and H. Chui, *J. Phys. D: Appl. Phys.*, 2018, 51, 385303.
7. X. Zhang, X. Qiao, W. Shi, J. Wu, D. Jiang and P. Tan, *Chem. Soc. Rev.*, 2015, 44, 2757–2785.

8. N. Bura, A. Bhoriya, D. Yadav, J. Singh and N. Sharma, *J. Phys. Chem. C*, 2021, 125, 18259–18269.
9. T. Tsujio, M. Oda and Y. Shinozuka, *Jpn. J. Appl. Phys.*, 2017, 56, 091001.
10. E. Hasdeo, A. Nugraha, M. Dresselhaus and R. Saito, *Phys. Rev. B*, 2014, 90, 245140.
11. M. Koshino and Y. Son, *Phys. Rev. B*, 2019, 100, 075416.
12. C. Chen, X. Chen, H. Yu, Y. Shao, Q. Guo, B. Deng, S. Lee, C. Ma, K. Watanabe, T. Taniguchi and J. G. Park, *ACS Nano*, 2018, 13, 552–559.
13. C. M. Chow, H. Yu, A. M. Jones, J. Yan, D. G. Mandrus, T. Taniguchi, K. Watanabe, W. Yao and X. Xu, *Nano Lett.*, 2017, 17, 1194–1199.
14. Y. Wang, C. Cong, C. Qiu and T. Yu, *Small*, 2013, 9, 2857–2861.
15. S. Pak, J. Lee, Y. W. Lee, A. R. Jang, S. Ahn, K. Y. Ma, Y. Cho, J. Hong, S. Lee, H. Y. Jeong et al., *Nano Lett.*, 2017, 17, 5634–5640.